# Power conversion and scaling for vanishingly small satellites with electric propulsion

by

George J. Hansel

Submitted to the Department of Aeronautics and Astronautics
in partial fulfillment of the requirements for the degree of

Master of Science in Aeronautics and Astronautics

at the

MASSACHUSETTS INSTITUTE OF TECHNOLOGY

June 2014





Signature redacted

Author .....
Department of Aeronautics and Astronautics
May 22, 2014

Signature redacted

Certified by .....
Paulo C. Lozano
Associate Professor of Aeronautics and Astronautics
Thesis Supervisor

Signature redacted

Accepted by .....
Paulo C. Lozano
Associate Professor of Aeronautics and Astronautics
Chair, Graduate Program Committee

**Power conversion and scaling for vanishingly small satellites with electric propulsion**

by

George J. Hansel

Submitted to the Department of Aeronautics and Astronautics
on May 22, 2014, in partial fulfillment of the
requirements for the degree of
Master of Science in Aeronautics and Astronautics

## Abstract

The development of ion electrospray propulsion systems (iEPS) as integrated microelectromechanical systems (i.e. MEMS) effectively miniaturizes propulsion for nanosatellites. Current iEPS thrusters consist of arrays of ion emitters, with a thruster for CubeSat application consisting of hundreds of emitters on a 1 $cm^2$ package. As a consequence, the lower bound on the size of satellites incorporating ion-emitter thrusters is not generated by the size of the thrusters themselves but the power supply they require: approximately 1700 volts at hundreds of nanoamps per emitter; a region in parametric space that is poorly explored in terrestrial power converters. We discuss the design and construction of a high-boost-ratio hybrid switched-magnetic/switched-capacitor power supply capable of powering small emitter arrays or single-emitter electrospray propulsion systems. In particular, we discuss the effects of and component requirements necessary for scaling the converter to the size and weight required for a board-level-integrated femtosatellite incorporating several single-emitter thrusters for propulsion and attitude control. This comprises scaling effects for physical and component parameters within a converter topology (such as operating frequency, parasitic effects, and component mass), but also motivates the choice of converter topology, as some are sensitive and others robust to miniaturization.

Thesis Supervisor: Paulo C. Lozano
Title: Associate Professor of Aeronautics and Astronautics

## Acknowledgments

I am exceptionally grateful to my family, my friends, and the professors in this department; all have provided me with the mentoring, help, advice, and kinship that made my experience at MIT what it was.

# Contents


**1 Introduction** **13**

1.1 Femtosatellites . . . . . 13

1.2 Electrospray and colloidal thrusters . . . . . 16

1.2.1 Existing power electronics approaches for electrospray thrusters . . . . . 18

**2 Hardware design** **23**

2.1 Hard requirements definition . . . . . 23

2.1.1 Notional satellite . . . . . 24

2.2 Implementation . . . . . 25

2.2.1 Scaling factors and topology selection . . . . . 25

2.2.2 Magnetics design and issues . . . . . 30

2.3 Communications . . . . . 32

**3 Software design** **35**

3.1 Maximum power-point tracking . . . . . 35

3.1.1 Quasi-DDRCC for hill-climbing policy evaluation . . . . . 36

3.1.2 DDRCC and quasi-DDRCC mode . . . . . 37

3.1.3 Test setup . . . . . 40

3.1.4 Concessions to non-ideality . . . . . 42

**4 Conclusion** **43**

# List of Figures

1-1 Schematic of the ion emission and acceleration across combined voltage $V_e$ (left) and higher-level integration of emitters into a thruster unit (right) in an iEPS electrospray thruster. Image from [1]. . . . . 16

1-2 Current is absolute value of the emitter current; symmetric due to the equivalence of positive and negative ion emission. Image from [1]. . . . . 17

1-3 The 2-CubeSat-card power supply unit for the existing iEPS systems described in the text and in [1, 2]. . . . . 18

1-4 The high-voltage switching stage of the iEPS power supply. The largest four components are the high-voltage MOSFETs (IXTH03N400 [3]). The light coloring and transparency of the board reflect its lack of internal layers to conform to IPC and other standards [4] for clearance and creepage, separating high voltage components from each other and traces at different potential. . . . . 20

1-5 Lower bound — taken at the limit of zero thermal impedance from junction to radiator — on the off-state junction temperature of the high-voltage FETs in the current iEPS power supply across a variety of sun intensities. . . . . 21

2-1 System-level representation of a power converter. . . . . 23

2-2 Mixed and intertwined propagation of constraints, from functional requirements (in red) to and among design features (in grey) for a power supply. . . . . 24

2-3 For scale, the notional femtosatellite next to a 1U CubeSat bus (left) and its front face (right). 1U CAD model from Pumpkin Inc. . . . . 25

2-4 The principal components of the existing voltage conversion stage for the iEPS PSU. In orange and yellow, the high-voltage Cockroft-Walton stages on each side of the transformer (in blue) secondary. In seafoam are the drivers of the primary transformer stage. A schematic is in Figure 2-5. . . . . 26

2-5 Implementation of iEPS PSU voltage conversion stage matches (with additional Cockroft-Walton steps) this reference implementation from [5]. . . . . 27
2-6 Schematic of a flyback converter [6]. . . . . 29
2-7 Our coils on PCB. Outer diameter of both coils is 25 mm. . . . . 30
2-8 Our coil capacitance problem. . . . . 31
2-9 Our coil capacitance problem, in schematic. Capacitance is not purely nodal: it's distributed across all the voltage gain of the secondary. . . . . 32
2-10 Schematic of our final converter. . . . . 32
2-11 Simulated voltage traces of our final converter during startup. Red is the first rectified stage; green the output to additonal C-W stages. Input 12V as in Figure 2-10. . 33
2-12 Key components of the final hardware solution: switch and gate driver (red), coil pair (blue), 4:1 switched-capacitor stage (green). . . . . 33

3-1 Idealized power/bias voltage curve of the PV simulator under test. . . . . 37
3-2 Schematic outline of major power components in test apparatus ($V_{oc}$ describes diode array, not current source) . . . . . 40
3-3 Test apparatus. MPPT is the black box in the center. . . . . 40
3-4 Tracking convergence to MPP, demonstrating a cycles-to-convergence consistent with the literature. Array voltage in orange; vastly undersampled PWM signal in turquoise. . . . . 41

# List of Tables

1.1 Summary of integration differences for femtosatellites. . . . . 14
1.2 Femtosatellite functional requirements. . . . . 15
1.3 Femtosatellite functional requirements, continued. . . . . 19
1.4 Femtosatellite functional requirements, continued. . . . . 22

2.1 Femtosatellite power supply functional requirements. . . . . 26

3.1 Femtosatellite software requirements. . . . . 35

# Chapter 1

# Introduction

A class of vanishingly small satellites called femtosatellites represents an interesting path forward in consumer accessibility to space [7] as well as low-cost distributed satellite systems. The Space Propulsion Laboratory has identified that microfabricated electrospray thrusters are a viable source of propulsion for these and similar satellites, but the restricting factor was the size of the high-voltage power supply required [8]. This work develops ultra-small power converters for use on vanishingly small satellites and demonstrates that such devices are intrinsically appropriate to the scale of such satellites and may be effective at even smaller scales.

## 1.1 Femtosatellites

The 1999 development of the CubeSat standard [9] established a standard set of requirements, guidelines, and suggestions for the development, launch, and deployment of satellites with a small form factor: linear dimensions on the order of 10 centimeters and mass on the order of 1 kilogram. The standard, along with the launcher/deployer specification from NASA [10], formalized the institution of SI-type prefixes to '-satellite' as an indicator of scale. Both specifications refer to CubeSats as "picosatellites," though other authors reflect the more common appellation of CubeSats (especially the multi-unit variety) as "nanosatellites," reserving 'pico-' to a slightly smaller class: between 100 grams and 1 kilogram, the specified maximum mass of a 1-unit CubeSat [11]. The discrepancy in terminology is not as severe as it may seem: while the 'classic' CubeSat may be a 1U falling into the picosatellite category, a preponderance of CubeSats launched or under development are the 3U type with masses 3 kilograms or more, falling under the nanosatellite category [12].

Table 1.1: Summary of integration differences for femtosatellites.

| Macrosatellite characteristic | ⟶ | Femtosatellite characteristic |
|---|---|---|
| bus-level integration | ⟶ | board-level integration [all] |
| board/component-level integration | ⟶ | die-level integration ("chip-sats": [17]) |
| mechanism actuation | ⟶ | sub-constellation reconfiguration [14, 16, 18] |
| active propulsion | ⟶ | passive propulsion or attitude control only [13, 15] |

Continuing the trend down the list of SI prefixes are "femtosatellites," with no standard defined but several authors concurrent on mass close to 10 grams and size and volume close to 10 $cm^2$ [11, 13, 14, 15, 16, 17]. Femtosatellites enter the literature as objects distinctly different from contemporary macrosatellites or even nanosatellites: while the nano/pico/CubeSat formulations begin with a size constraint and adopt architectures consistent with much larger satellites in order to support a mission requirement, femtosatellites begin with the capability achievable exclusively from board-mounted electronics and seek missions appropriate to that capability, as in [14, 16, 18]. The primary capability of femtosatellites is not an operational one but is simply the capability to be manufactured and launched in mass at trivial cost: this capability is a core enabler of proposed or executed femtosatellite missions which almost uniformly involve "swarms" [18] of femtosatellites.

In Table 1.1 we summarize the key architectural (i.e. integration-style) differences between macrosatellites, including CubeSats, and femtosatellites. The differences fundamentally stem from the presence of a bus structure to which mostly independently-operating subsystems are integrated in the case of the former and the fact that the highest level of integration is only as an element in a constellation in the case of the latter. In other words: the highest level of on-orbit integration is synthetic rather than mechanical. Subcomponents found on CubeSats, such as magnetic torquers or communications cards or wire harnesses, are replaced, if possible, with whatever can be duplicated with printed traces on a circuit board [13] or metallization in a die-level integrated circuit [17].

While we have identified that the promise of femtosatellite missions is in the reconfigurability and density of their on-orbit configurations, and that the manufacturing processes undertaken for femtosatellites are capable of the mass production those configurations entail, what remains missing from the literature and the practice is actuation consistent with this function. The first launched femtosatellite mission, the crowd-funded "KickSat" project [7], was a dis-

Table 1.2: Femtosatellite functional requirements.

| Number | Type | Requirement | Justification |
|---|---|---|---|
| 1 | Actuation time scale | Faster than LEO orbit period | Null relative motion |
| 2 | Operability | Consistent with proximity | Asserted |
| 3 | Manufacturing | Board-level or lower | Asserted |

penser designed to release its Sprite femtosatellites without position sensing, attitude control, or propulsion. While the assumption of attitude control through board-mounted magnetic torquers is a common one, considerations of propulsion systems necessary to maintain a close constellation [19] are rare. Two methods have been proposed: passive propulsion by solar radiation pressure [20] and Lorentz propulsion [21]. The first method has merit in some environments but is not generally accessible in low-Earth orbit, due to the relative dominance of aerodynamic forces [22, 23]. The second method, which is a small-scale version of an electrodynamic tether, may also be effective at some altitudes excluding LEO but requires geometric properties (e.g. a metallized sphere on the scale of the satellite) that are not consistent with a femtosatellite and board-level-integrated approach. Furthermore, operating satlets with strong electric dipole moments may not be consistent with certain constellation configurations. To avoid intersatlet dipole attraction, for example, it may be necessary to prohibit constellations with characteristic spacings less than the Debye length of the local plasma which above the ionosphere exceeds tens of meters [23].

In this discussion we have unlocked a few requirements important to the scaling considerations for femtosatellites and their features. We need to maintain sufficient actuation on time scales relevant to the operation of the constellation and we require that the actuation maintaining this operation is consistent with the closeness of the adjacent satellites: proximity operations.

It is clear that these two requirements are linked: the larger the characteristic spacing $\Lambda$ of the constellation the greater the actuation is required to be. For an orbit with period $T$, we define the characteristic relative velocity $\mathcal{V}$ in the local vertical/local horizontal frame for satlets in a constellation of characteristic spacing $\Lambda$ as $\frac{\Lambda}{T}$. By a similar argument, the characteristic relative angular velocity $\mathscr{A}$ is $\frac{2\pi}{T}$. To satisfy our actuation and operability requirements, it's necessary to actuate with a strength resulting in speeds greater than these and to satisfy our manufacturing requirement it must be integrable directly onto a printed circuit or indirectly on a die subsequently bonded to the circuit substrate.

## 1.2 Electrospray and colloidal thrusters

A propulsion method with the ability to meet all of these requirements is a microfabricated electrospray thruster as described in [1]. Electrospray thrusters are directed ion emitters whose thrust is generated by the reaction of a static electric field with ions ejected from a source onboard the satellite. Shown in Figure 1-1, ion emission in electrospray thrusters is the result of an ionic and therefore conductive liquid interacting with the electric potential between a charged grid, which ideally does not touch the liquid, and an oppositely charged needle (the "emitter"), from which the liquid is drawn. The needle breaks the plane symmetry of the charged grid and concentrates electric field near its tip (radius near 5 $\mu$m [1]), which pulls the meniscus of the liquid covering the tip into a "Taylor cone", an almost-perfectly-conical structure with a very sharp tip [24]. The tip of the Taylor cone concentrates the electric field to the extent that the field external to the liquid dominates the inter-ionic surface tension forces and the meniscus locally disintegrates. For a completely ionic liquid — the room-temperature molten salt EMI-$BF_4$, in [1, 25] and others — like the propellants, this disintegration is the ionization process, requiring only 5-8 eV in some experiments [1]. With a positively charged grid, the freed negative ions above the tip accelerate through the grid, generating thrust, while the positive ions are drawn back into solution.

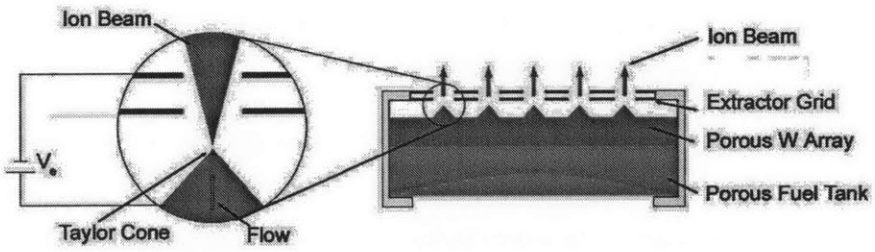


Figure 1-1: Schematic of the ion emission and acceleration across combined voltage $V_e$ (left) and higher-level integration of emitters into a thruster unit (right) in an iEPS electrospray thruster. Image from [1].

This is a process with many competing physical effects[1] directly affecting the density, distribution, and mass-to-charge ratio of the majority carrier so there is no applicable analog to the Shockley diode equation, relating the applied voltage $V_e$ to the device current. However, experimental studies of the I-V characteristics of these sources have been performed, summa-

[1] Electrochemistry at the emitter, electrochemistry within the plume, occasional presence of multiple Taylor cones per emitter, density of and potential relative to the ambient plasma ...

rized in [1] and excerpted in Figure 1-2, and are sufficient characterization of these devices for the purpose of designing a power supply. The high incremental resistance (tens to hundredths of gigohms per emitter) relative to the active devices allows us to regard this very much like a high-voltage, low-carrier-density diode.

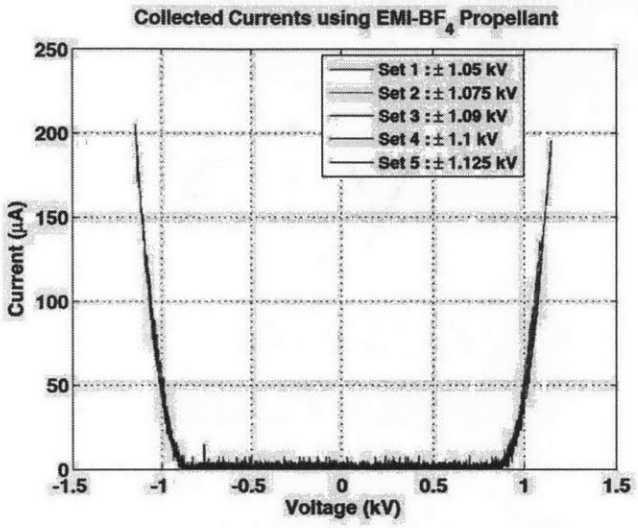


Figure 1-2: Current is absolute value of the emitter current; symmetric due to the equivalence of positive and negative ion emission. Image from [1].

Variations in the size of the emitter and the way the ionic liquid propellant reaches the tip mean that different authors achieve different thrusts per emitter: emitters in [25] produce micronewtons per emitter while the iEPS system of [1, 2] produces close to 100 nanonewtons of thrust at a current of 100 nA.[2] Macroscopic thrust, for CubeSats and larger, is produced by microfabricated arrays of hundreds of emitters. This "arrayed" arrangement is what inspires our argument's shift toward scaling: it is only linearly more difficult to produce more thrust from additional emitters and linearly easier to produce smaller thrusters, appropriate to a femtosatellite, with fewer emitters. Very simply, our goal is to determine whether that can also be true of the voltage converter than those emitters, even down to a single-emitter thruster, can satisfy the same condition.

[2] $I_{sp}$ and thrust vary with current and voltage: the precision of that adjustment is one benefit to electrospray thrusters. However, at certain voltages, currents, and emitter configurations/materials, electrochemical reactions and instability of the Taylor cone structure serve to limit both the peak and the minimum thrust of the device.

### 1.2.1 Existing power electronics approaches for electrospray thrusters

The electrospray propulsion system under current development, called iEPS, at MIT's Space Propulsion Laboratory is a platform targeted at propulsion of CubeSats down to 1U. It uses 2000 emitters distributed on 4 MEMS-fabricated thruster chips, consuming a total near 15 watts. Of prime interest is the power supply unit pictured in Figure 1-3.

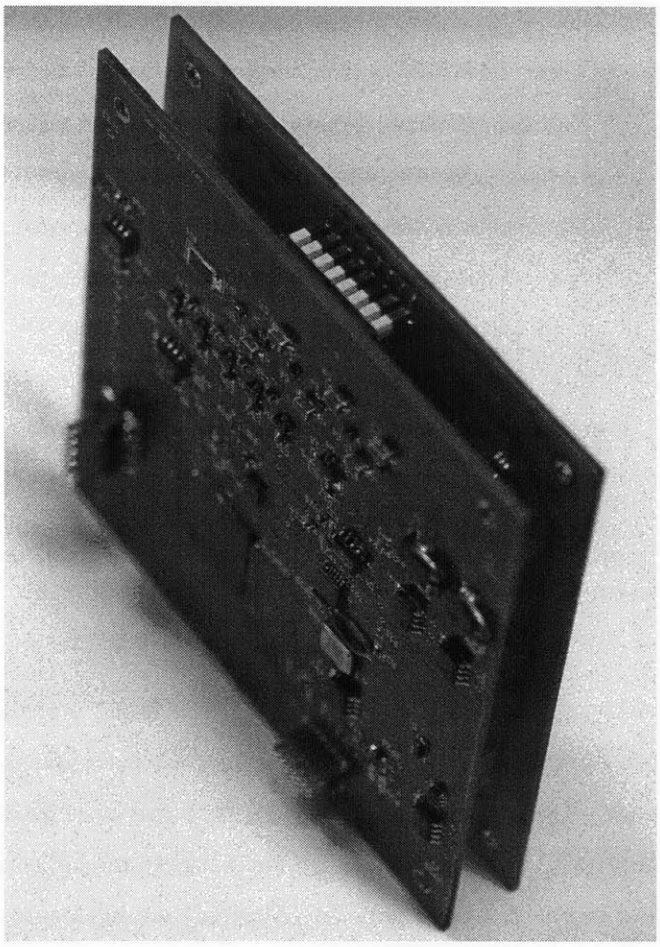

Figure 1-3: The 2-CubeSat-card power supply unit for the existing iEPS systems described in the text and in [1, 2].

The power supply unit (PSU) consists of two CubeSat-form-factor boards of 10 cm by 10 cm, stacked and interspersed with control electronics. The power density of this unit is about 30 $cm^3/W$ and it has a conversion efficiency from 5 to 1800 volts near 70% [1]. Of the roughly 200 $cm^3$ that it occupies, roughly half supports the single-supply voltage conversion and the remaining half is composed of high-voltage MOSFETs [3] and the buffers necessary to drive them.

Table 1.3: Femtosatellite functional requirements, continued.

| Number | Type | Requirement | Justification |
|---|---|---|---|
| 4 | Input voltage | Match satellite bus | Compatibility |
| 5 | Output voltage | 1800 volts | Fixed by emitter type |
| 6 | High-voltage switching | Must ensure neutrality | Eliminates charging |
| 7 | Optimization objectives | May include "per terminal" | Flows from 6. |
| 8 | Output current | 500 nA per emitter | Device value [2] with headroom. |

Switching of the exciting polarity *by some means* at the thruster terminals is necessary for alternation of the thruster polarity to ensure an electrically-neutral satellite. Ejecting all negative ions or all positive ions would charge the satellite, so the PSU must be able to alternate the beam polarity either in time or across the four thrusters. Why is the switching on the high side? Because this choice of topology makes the generation of high voltage, per discrete or isolated source, incrementally more expensive in mass and volume than the high-voltage switching hardware required to compensate. The mass and volume cost of the voltage conversion stage is perceived to dominate the mass and volume cost of the high-voltage-switching stage.

We examine whether the iEPS PSU topology and approach to power conversion is a viable approach for a femtosatellite constellation in the next chapter.

This discussion has generated some additional requirements for femtosatellite power supplies, so we make them explicit in Table 1.3. Of the four, the "Optimization objectives" entry requires the most explanation. Requirement 7 captures the fact that an optimization objective like "greatest output power per unit mass" is not consistent with a broader view that includes the high-voltage switching Requirement 6: four power supplies with a mass of 20 grams, each capable of alternating polarity, are, collectively, more useful than a single power supply of mass 60 grams able to power all four thrusters but unable to alternate polarity effectively. *Total power and specific power is in some sense secondary.* This is a nonintuitive result that appears again in the scaling principles for the notional femtosatellite in Section 2.1.1.

There are some intrinsic device problems with high-voltage MOSFETs, as well. In particular, the high-voltage FET pictured in Fig. 1-4 on the iEPS PSU has a positive thermal coefficient of saturation leakage current $I_{dss}$, leaking 10 $\mu$A at 25°C but 750 $\mu$A at 125°C [3]. This leakage is not atypical for a power FET, but the extremely high voltage that the leakage current crosses makes the energy dissipation here quite high: 1800 V × 750 $\mu$A = 1.35 watts. Supposing that each FET is driven several times above the rating of the iEPS thruster, to 5 mA: it dissipates only 7.25

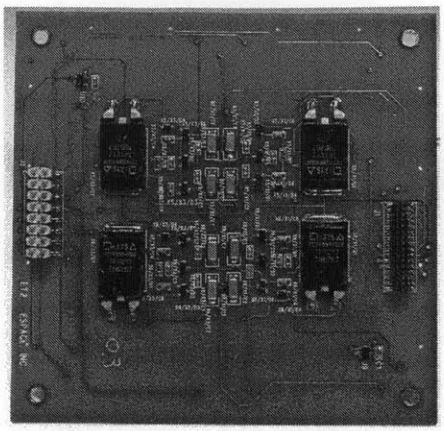

Figure 1-4: The high-voltage switching stage of the iEPS power supply. The largest four components are the high-voltage MOSFETs (IXTH03N400 [3]). The light coloring and transparency of the board reflect its lack of internal layers to conform to IPC and other standards [4] for clearance and creepage, separating high voltage components from each other and traces at different potential.

milliwatts across the 290 ohm $R_{ds_{on}}$. At elevated temperatures, this switch dissipates hundreds of times more power while off than while on, which is explained by the fact that the leakage current at this temperature exceeds the iEPS thruster current.

Femtosatellites have effectively no capability for thermal management with the exception of attitude control. It would be useful to know if this high-leakage phenomenon still supports operation in an environment where equilibrium temperatures are determined by radiative balance. To support this, we construct a simple thermal model of the junction temperature:

$$A_{rad}\sigma\left(T_{rad}^4 - \int_{view} T_{view}(\mathbf{s})^4 d\mathbf{s}\right) + c\frac{dT_{acc}}{dt} = V_{ds}I_{dss}(T_{junc}) \tag{1.1}$$

This model features four distinct temperatures: a function describing the temperature of the objects in view at a particular solid angle $\mathbf{s}$ $T_{view}(\mathbf{s})$, the radiator temperature $T_{rad}$, an accumulator temperature $T_{acc}$, and a junction temperature $T_{junc}$. To generate absolute lower bounds on the junction temperature in operation, we set $T_{rad} = T_{acc} = T_{junc}$: the radiator rejects as much as possible and the entire accumulator is isothermal to the junction. Simulating a LEO environment, we model a radiator with unit emissivity at the satellite temperature, a 300°K Earth in half the view and radiator emissivity of 0.4 to the solar spectrum, and neglect other radiative sources.

Without the precise curve for the saturation leakage current, we construct a first-order ap-

proximation to have some estimate of the device leakage at various temperatures at the specified (by our requirements, not the device datasheet) $V_{ds}$:

$$I_{dss}(T_{junc}) = \begin{cases} 10^{-6}[10 + 74(T_{junc} - 298)] & T_{junc} \geq 298 \\ 10^{-5} & T_{junc} < 298 \end{cases} \tag{1.2}$$

where the junction temperature $T_{junc}$, as before, is taken in Kelvin. The resulting contours of equilibrium temperature for various radiator sizes and effective solar intensities are in Figure 1-5.

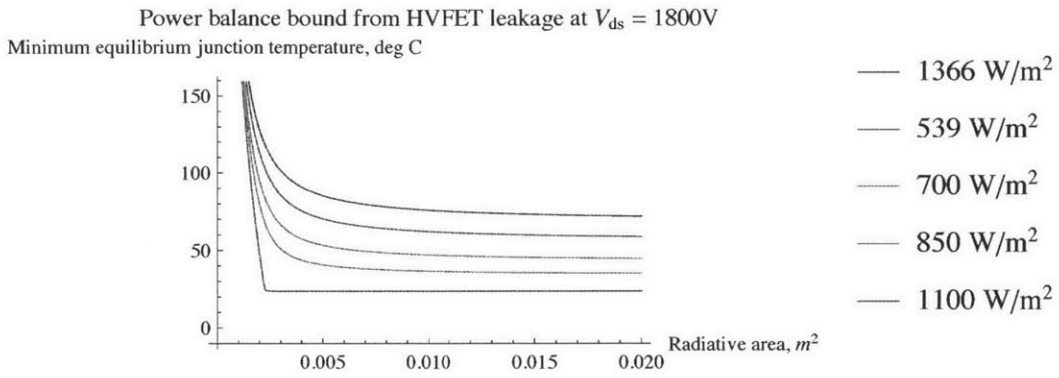


Figure 1-5: Lower bound — taken at the limit of zero thermal impedance from junction to radiator — on the off-state junction temperature of the high-voltage FETs in the current iEPS power supply across a variety of sun intensities.

Above a certain magnitude of effective solar intensity, the device develops a critical minimum radiator area about 0.0022 square meters: a one-sided square just under 5 cm on a side. Around and below this critical radiator area, the minimum operating junction temperature is extremely sensitive to radiator size and effectively 'runs away'. This is not an acceptable design condition, and its fundamental enablers (high bias voltage combined with a positive thermal coefficient of saturation leakage current) are intrinsic to the chemistry: it's a problem that will change in magnitude with differently-sized switches, but will never go away. For this reason and also those outlined in the justifications for the "Optimization objectives" requirement, we prohibit the use of active high-voltage switches, captured in Table 1.4.

Table 1.4: Femtosatellite functional requirements, continued.

| Number | Type | Requirement | Justification |
|---|---|---|---|
| 9 | Active HV switches | None permitted | Incompatible with lack of thermal control |

# Chapter 2

# Hardware design

In this chapter we discuss the physical and electrical design of a power supply for an electrospray-propelled notional femtosatellite as well as the scaling factors of each of the components, implementing a scaled-up version as proof of concept. We begin by developing the requirements the supply/satellite must satisfy by flowing down from the requirements we generated in Section 1.1, Table 1.2 to requirements on specific physical and electrical characteristics, and verify each requirement by either design or experiment. In particular, the need to develop requirements with careful attention exists because of counterintuitive results of scale: for example, the primacy of certain requirements makes conversion efficiency only a secondary feature of an optimization objective.

## 2.1 Hard requirements definition

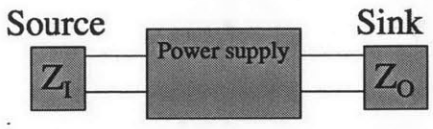


Figure 2-1: System-level representation of a power converter.

A power supply is, at a system level, a fairly simple device: two ports, input and output. Associated to each port are the impedance characteristics $Z_I$ and $Z_O$ respectively; the two may be functions of some larger state, including time. With a sufficient behavioral description of the power converter, this representation is enough to compose a complete equation of state for the device. The extent of behavioral description that represents sufficiency is exactly the set of

requirements we need to generate in this section.

As a general statement, the fact that one interacts with the power supply *only* as a two-port device with essentially no external expression of the internal state means that each functional requirement (e.g. output voltage) will propagate to the internal design features (e.g. inductor core material) with an effectively arbitrary mapping, which we show in Figure 2-2. Fortunately, some design features are 'special': they correspond to physically-conserved quantities which are implementation-agnostic like energy, or practically-universal characteristics.

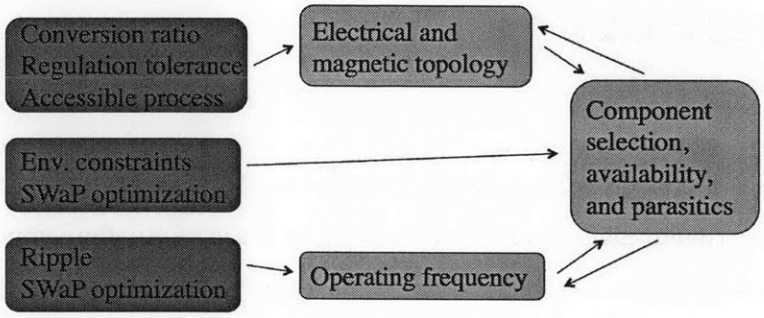


Figure 2-2: Mixed and intertwined propagation of constraints, from functional requirements (in red) to and among design features (in grey) for a power supply.

One such universal characteristic in power conversion is that of a cyclic operation: the converter stores energy for part of a cycle by transducing energy into electric or magnetic field, and for the rest of the cycle transduces energy back from the field in a different form e.g. at a different voltage. This explains the division in Figure 2-2 of design features into "topology" and "frequency" components: regardless of the path through the state space taken by a cyclic process and agnostic even of what the state space represents, a cyclic process can be repeated at any speed.

### 2.1.1 Notional satellite

In developing the power supply for a femtosat-scale iEPS and verifying its conformance to requirements, we will assume a notional femtosatellite as a baseline, pictured in Figure 2-3 next to a 1U CubeSat bus.

The specifications of the notional satellite are simple:

- Printed-circuit-compatible substrate, 30 mm by 30 mm by 1 mm.
- In each of four corners, a single-emitter electrospray thruster powered by its own supply.

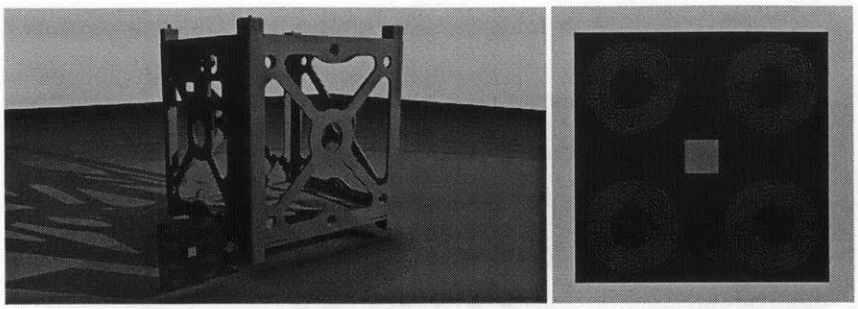

Figure 2-3: For scale, the notional femtosatellite next to a 1U CubeSat bus (left) and its front face (right). 1U CAD model from Pumpkin Inc.

- Control electronics in the center.
- All available surfaces covered with monocrystalline silicon solar cells: about 15 $cm^2$.
- No bulk energy storage.
- Mass under 15 grams.

We now state the requirements, including additional satellite-derived requirements all together in Table 2.1.

## 2.2 Implementation

### 2.2.1 Scaling factors and topology selection

What about the topology on the existing iEPS PSU? Can it scale to the extent required? In Figure 2-4 we've isolated the active components of the 5V-to-1800V converter onboard the PSU.

Somewhat universally, a power converter can be divided into energy storage elements and configuration-changing elements - switches. Division of power converter elements into those which store energy and those which change configuration is a topology-independent decomposition that allows us to examine the scaling for the two energy storage components of the voltage stage for the iEPS PSU.

Let's consider scaling factors, first for the transformer component. With $n_{pri}$ the number of turns on the primary, $I_{max}$ the peak current, and $B_{max}$ the saturation field strength of the core material, the transformer is sized (assuming mass proportional to volume) to avoid saturation at

Table 2.1: Femtosatellite power supply functional requirements.

| Number | Type | Requirement | Justification |
|---|---|---|---|
| 1 | Actuation time scale | Faster than LEO orbit period | Null relative motion |
| 2 | Operability | Consistent with proximity | Asserted |
| 3 | Manufacturing | Board-level or lower | Asserted |
| 4 | Input voltage | Match satellite bus | Compatibility |
| 5 | Output voltage | 1800 volts | Fixed by emitter type |
| 6 | High-voltage switching | Must ensure neutrality | Eliminates charging |
| 7 | Optimization objectives | May include "per terminal" | Flows from 6. |
| 8 | Output current | 500 nA per emitter | Device value with margin |
| 9 | Active HV switches | None permitted | Lack of thermal control |
| 10 | Average input power | 200 mW typ. | Array area limit |
| 11 | Average input power | 200 mW typ. | Array area limit |
| 12 | Input ripple | <5% total | Typical $\mu$C tolerance |
| 13 | Output ripple | <10% below $1/T_{transit}$<br>Above $1/T_{transit}$, no limit | Allow monochromaticity |
| 14 | Conversion efficiency | None required | Large power margin |
| 15 | Voltage stress | Compatible with CMOS | Permit required $f_{sw}$ |

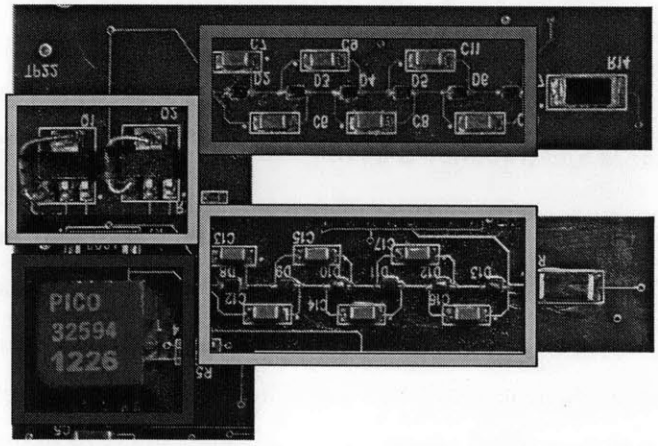


Figure 2-4: The principal components of the existing voltage conversion stage for the iEPS PSU. In orange and yellow, the high-voltage Cockroft-Walton stages on each side of the transformer (in blue) secondary. In seafoam are the drivers of the primary transformer stage. A schematic is in Figure 2-5.

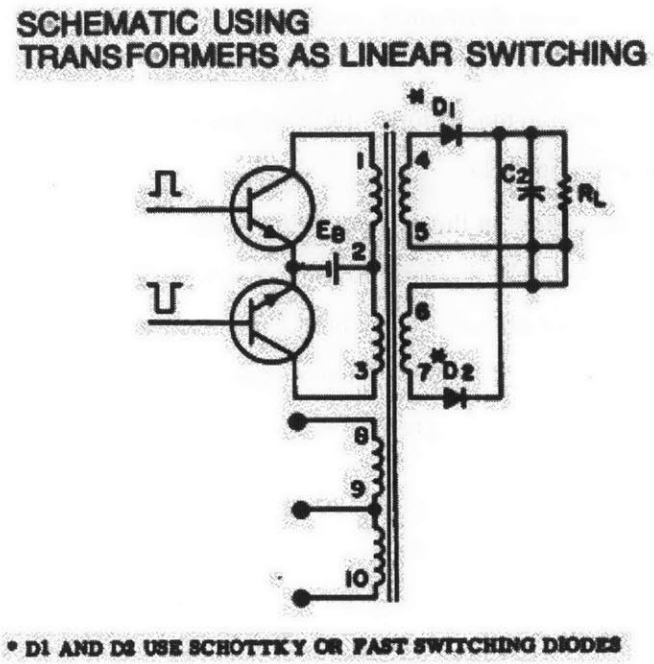


Figure 2-5: Implementation of iEPS PSU voltage conversion stage matches (with additional Cockroft-Walton steps) this reference implementation from [5].

peak current, expressed as:

$$n_{pri} I_{pri} \mu_{core} \leq \Phi_{max} = B_{max} A_{core} \tag{2.1}$$

where $A_{core} \propto V_{core}^{\frac{2}{3}}$ is the cross-sectional area of the core. Secondarily the transformer is scaled to accommodate the necessary number of turns. Altogether, this defines scaling relations between the mass and the input power, the inductance, the operating frequency, and the conversion ratio.

Input power:

$$m_{trans} \propto P_{in}^{\frac{3}{2}} \tag{2.2}$$

Inductance:

$$m_{trans} \propto L^3 \tag{2.3}$$

Operating frequency at constant quality factor [26]:

$$f_{sw} \propto m_{trans}^{-\frac{2}{3}} \propto \frac{1}{P_{in}} \tag{2.4}$$

So we can note that a set of distributed converters handling the same total power will have a total mass lower than a single larger converter. So the nonintuitive results from Section 1.2.1 are again reinforced: we should make more, smaller supplies, whenever possible, up to the maximum switching frequency possible.

Moving on to the capacitors in the existing iEPS system. Capacitors in this type of voltage multiplier configuration — a classic Cockroft-Walton generator [27] — are in a 'slow switching limit' where the switching period is much longer or comparable to the RC time constant for charging. The energy transfer per cycle is a large fraction of the energy capacity of each capacitor before dielectric breakdown. For capacitors with density $\rho$ and dielectric breakdown strength $D_{brk}$:

$$\frac{P_{in}}{f_{sw}} \propto \frac{m_{cap}}{\rho} D_{brk} \tag{2.5}$$

To give a sense of size, $D_{brk}$ for common capacitor dielectrics is about 0.6 mJ/cm$^3$, which yields on the order of 1 cm$^3$ of capacitors for the iEPS PSU. As before, slight manipulation yields scaling relations.

Input power:

$$m_{cap} \propto P_{in} \tag{2.6}$$

Operating frequency:

$$m_{cap} \propto \frac{1}{f_{sw}} \tag{2.7}$$

Conversion ratio is bounded not by volume but by number of capacitors. A supply with $n$ capacitors bounds the conversion ratio to the $n$th Fibonacci number [28].

Applying these scaling factors, an appropriately-sized, identical topology power converter meeting our requirements at 1000 times less power output would feature a transformer of mass 160 *micrograms*, operating frequency 30 MHz (from 30 kHz), and 2 milligrams of capacitors, and preserve the low voltage stress on the input switches. Is that an acceptable solution?

Not by far. While we have shown the parametric scalings, we haven't shown the scalings of parasitic parameters or ensured consistency with physical properties. For example, consider the generalized Steinmetz equation for the power dissipated in the core [29]:

$$P_{core}(t) = k_i \left[ \frac{d|\mathbf{B}|}{dt} \right]^a |\bar{\mathbf{B}}|^{b-a} \tag{2.8}$$

The parameters $k_i$, $a$, and $b$ vary with material but both $a$ and $b$ exceed unity: power losses in

the core hugely increase with frequency. The core materials with acceptable losses at 30 MHz have far lower $\mu$ and would require increases in core size, though high-frequency core materials are an active area of research, as in [30, 31].

So we need to choose a different topology than that in the iEPS voltage conversion stage of the PSU, and that means seeking an alternate topology, compatible with high frequencies and coreless inductors.

We selected a flyback topology in order to demonstrate effectiveness of the magnetics with the minimum count of active switches. The flyback topology, pictured in Figure 2-6, is a pretty flexible topology, offering resonant, continuous, and discontinous conduction modes [32]. The distinctive feature of the flyback topology is the change in the sizing feature when the core is removed. The transformer is then a purely energy storage element, rather than an energy-transmission element because current in the secondary, regardless of the operating mode of the primary, *isn't* continuous. So the sizing criterion changes from 'avoid saturation' to 'store sufficient cyclic energy', just like a capacitor.

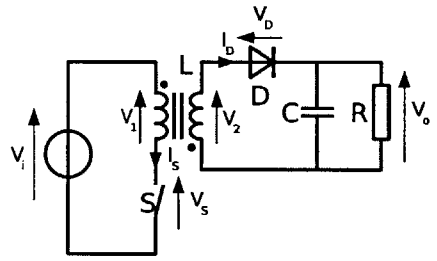


Figure 2-6: Schematic of a flyback converter [6].

The low-voltage-stress switch was picked to be a gallium-nitride FET to comply with our thermal requirement: GaN has one of the wider temperature ranges of available high-speed semiconductors. From the limited selection of GaN FETs commercially available, we picked the EPC2012, as it is the lowest-gate-charge such power FET available and would permit the fastest switching. The manufacturer also claims some radiation hardness [33]. We operated this switch at 4 MHz.

The rectification stage of the flyback converter can consist of any arrangement of Cockroft-Walton stages and does not represent any significant novelty, so we engaged most of all with the design of the magnetic structures.

### 2.2.2 Magnetics design and issues

For consistency with Requirement 3, we designed planar, printed magnetics at a scale approximately 200% of the scale of the notional femtosatellite, sized to the 150 $\mu$m minimum feature and space size of inexpensive prototype circuit manufacturers. Shown in Figure 2-7, these are very plain magnetics: a planar connectivity constraint, a minimum feature size constraint, and the objective of maximum self-inductance yields only one configuration. The primary and secondary coils, at a 1:10 turns ratio, are patterned identically and are connected only slightly differently at the midpoint. We measured the 20-turn secondary to have an inductance of 11 $\mu$H.

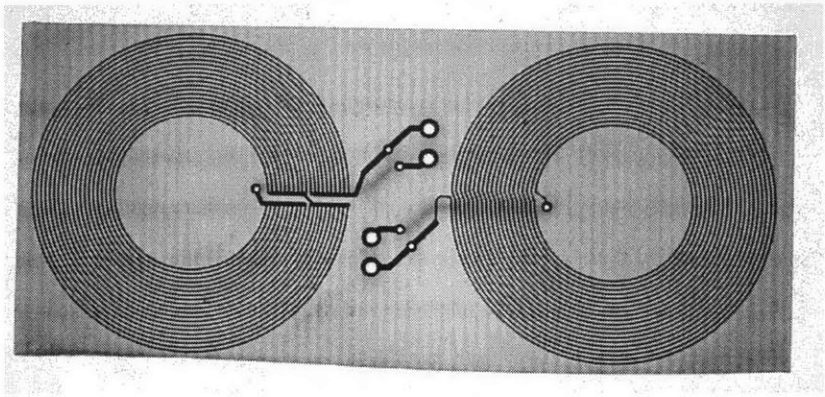

Figure 2-7: Our coils on PCB. Outer diameter of both coils is 25 mm.

The skin depth of copper at 4 MHz is 32.8 microns, a fifth the thickness of each trace. While the DC resistance of the secondary is 1.2 ohms, the AC resistance of the fundamental switching frequency exceeds 10 $\Omega$. As the switching signal is not sinusoidal, the effective AC resistance exceeds that, for a significant resistive loss tangent $> \tan \frac{10}{11\mu * 2\pi * 4M} \approx \tan \frac{1}{27.6}$ in operation.

An effective transformer requires good coupling — a high proportion of total flux being shared by both windings — between the primary and the secondary coils. Close coupling is crucial to high voltage gain in the transformer stage of a flyback converter as the voltage gain is precisely the ratio of the secondary to the primary flux. In cored transformers, this is achieved because the high permeability of the core confines the field there. In coreless transformers, coupling suffers. Fortunately, planar magnetics may be placed extremely close together, separated only by the insulation necessary to prevent shorting, and the coupling in this case is consistent with near-unity: >0.8 based on our comparison of SPICE results with measurements.

However, the need for close coupling of primary to secondary introduces a problematic par-

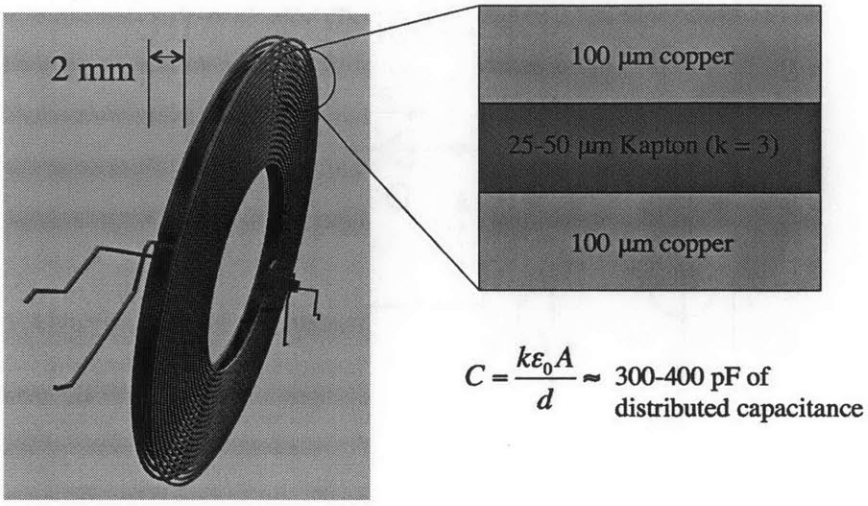


Figure 2-8: Our coil capacitance problem.

asitic effect between the nominally-isolated windings of the flyback converter: capacitive 'injection', a continuous, distributed high-frequency short between the primary and the secondary which severely harms voltage gain. Figure 2-8 depicts the magnitude of this problem: the capacitive impedance from the secondary to the primary and back is close to the inductive impedance of the secondary itself. The voltage gain is reduced because the secondary has shorted against itself across the primary.

Worse, the parasitic interlaminar capacitance scales exceptionally poorly, being more significant at smaller scales than larger ones:

$$\frac{L}{C} \propto (scale)^{-1} \tag{2.9}$$

This isn't a problem in low-output impedance applications or low-frequency ones [34], but our frequency and output impedance are necessarily quite high.

This problem is addressed in a somewhat novel modification to the flyback topology, shown in Figure 2-10: we short the switch side of the primary to the high side of the secondary. In effect this becomes a boost converter with an inductive voltage divider/multiplier rather than an inductor. The switch turns on to energize the field in the inductor, and when the switch turns off, the decreasing current boosts the voltage on the inductor output. While we would choose output rectifier components in a boost converter to minimize output ripple, the output here has

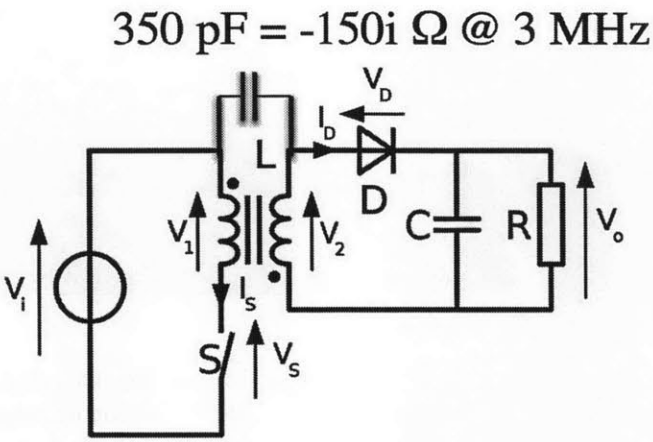


Figure 2-9: Our coil capacitance problem, in schematic. Capacitance is not purely nodal: it's distributed across all the voltage gain of the secondary.

very high ripple which is ideal for driving the subsequent switched-capacitor multiplier stages.

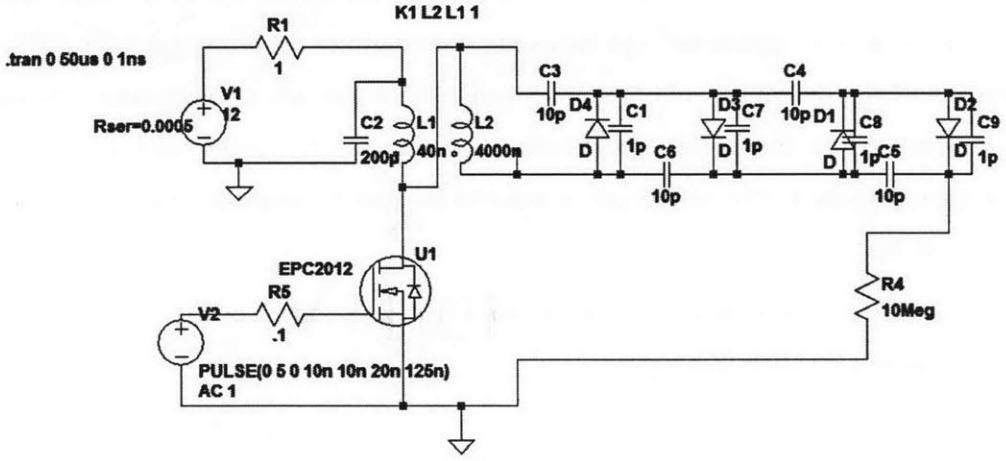


Figure 2-10: Schematic of our final converter.

## 2.3 Communications

Though the coils we use are quite small for power conversion and the frequencies quite high for power conversion, the 4 MHz frequency of our scaled-up demonstrator corresponds to a 75 meter wavelength (compare: 25 mm coil). Skin and proximity effect losses can be compared with the radiative loss by computing the effective far-field radiation resistance of this loop antenna

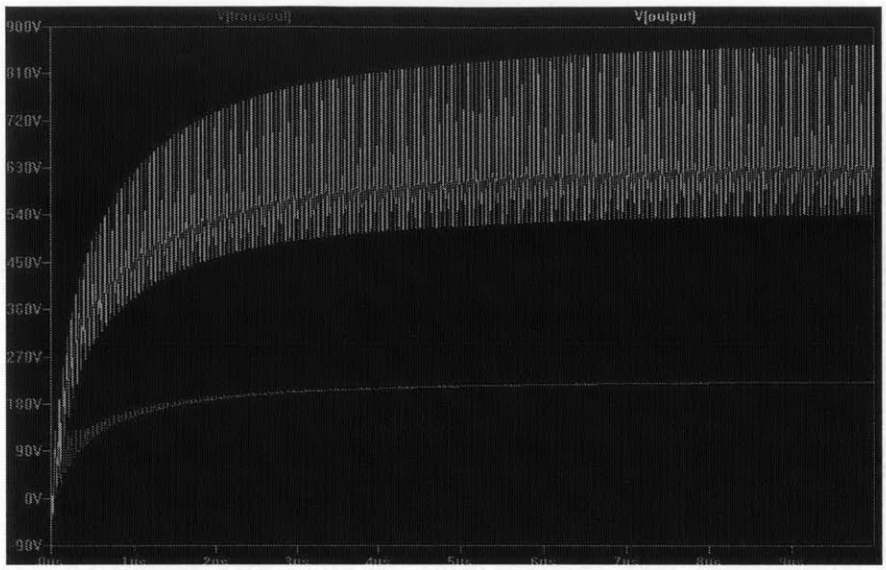


Figure 2-11: Simulated voltage traces of our final converter during startup. Red is the first rectified stage; green the output to additonal C-W stages. Input 12V as in Figure 2-10.

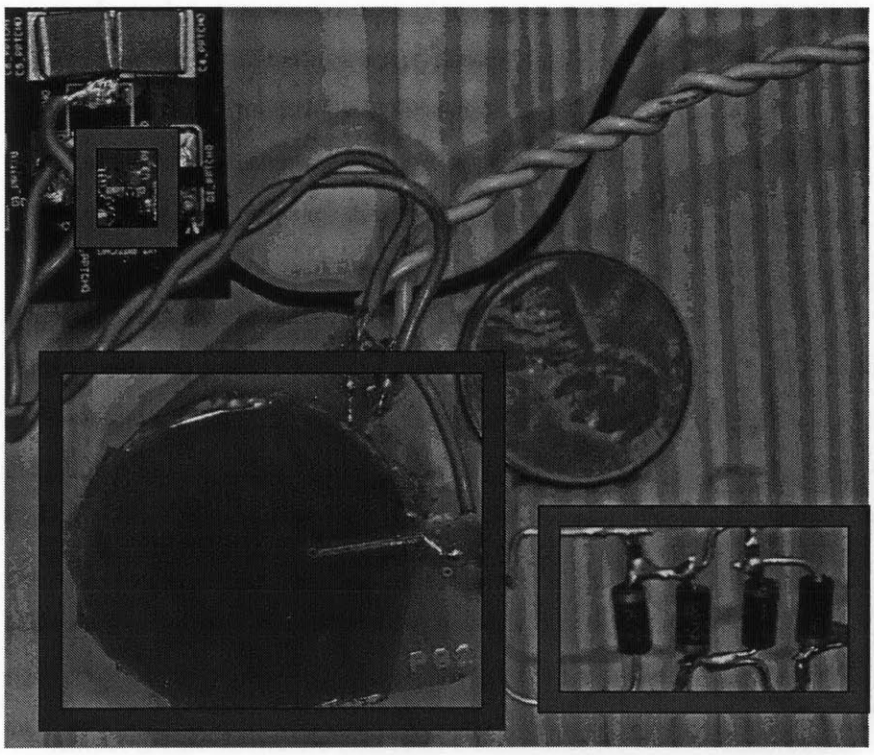

Figure 2-12: Key components of the final hardware solution: switch and gate driver (red), coil pair (blue), 4:1 switched-capacitor stage (green).

with area $A$, from [35]:

$$R_{rad} = 320\pi^4\left(\frac{A^2}{\lambda^4}\right) \tag{2.10}$$

$$= 9.75 \times 10^{-11}\Omega \tag{2.11}$$

A 100 milliampere RMS sinusoidal drive on the primary, therefore, results in an emitted far-field radiated power of -90.1 dBm.

However, our prox-ops requirement ensures that the far-field characteristics, past several times the 75 meter wavelength of interest, are irrelevant. We can compute the near-field coupling $K$ at range 1 meter between a primary and an adjacent secondary, with the coils parallel and in-plane. The H-field in the plane, for a primary with dipole moment $\mathbf{m}$, is:

$$\mathbf{H}(r) = -\frac{1}{4\pi}\frac{\mathbf{m}}{r^3} \tag{2.12}$$

The mutual inductance is simply the ratio of the induced flux to the inducing current, so

$$L_m \approx \frac{\frac{2I_{primary}}{4\pi}\frac{A_{loop}}{r^3}}{I_{primary}} \tag{2.13}$$

$$\approx \frac{2 \times 20\text{cm}^2}{4\pi(1\text{m})} \tag{2.14}$$

$$\approx 1.2\,\text{nH} \tag{2.15}$$

1.2 nanohenries is about $\frac{1}{10000}$ of the free inductance of the secondary. Correspondingly we can expect $\frac{1}{10000}$ of the output voltage that the primary is inducing in its intended secondary to appear in the secondary of a femtosat 1 meter away. That's 180 mV: well above the threshold voltage of the onboard comparators in the microcontrollers in Chapter 3. This yields an interesting side-effect: we have essentially free communications with adjacent satellites, by on-off keying the primary.

# Chapter 3

# Software design

By both design and requirement (number 2), the voltage converter described in Chapter 2 will never operate 'alone'. It will

- always operate in a constellation,
- to support Requirement 2 it will have some understanding of the state of other parts of the constellation, and
- by the arguments in Section 2.3, always have inexpensive near-field communications with the rest of the constellation,

so we flow this into additional requirements in Table 3.1.

In this chapter, we discuss and demonstrate one of the feedback loops that can be closed by integrating sensor data over the constellation: tracking of the solar array bias for maximum power output.

## 3.1 Maximum power-point tracking

Active optimization of the bias voltage of photovoltaic modules (maximum-power-point tracking) is a topic of considerable academic and practical interest [36] for terrestrial systems as well

Table 3.1: Femtosatellite software requirements.

| Number | Type | Requirement | Justification |
|---|---|---|---|
| 16 | State estimation scope | Global to constellation | Assure Req. 2 |

as space- or air-borne ones simply because the power gains are so high and despite the low incremental cost of ground power capacity. One method of MPP tracking, digital dithering ripple correlation control, is developed in [37] and demonstrated further on a purpose-built buck MPPT in [38]. For this project we implemented a DDRCC method on an existing boost MPPT[1] that had previously implemented a conventional perturb-and-observe [36] tracking algorithm.

### 3.1.1 Quasi-DDRCC for hill-climbing policy evaluation

The term 'quasi-DDRCC' emerges in our case as a consequence of hardware limitations and the degeneracy of various tracking schemes at time scales other than that for which they were designed. In particular, plain ripple correlation control and DDRCC share a feedback mechanism, but differ — other than in their processing and actuation — only in the timescale of the ripple they sense. The property that RCC and DDRCC both share is that the characteristic frequency of the control and the sensed ripple $f_{ctl}$ exceeds the characteristic frequency of the array-side filter $f_0 = \frac{1}{2\pi\sqrt{LC}}$. In the case of RCC this is obvious as $f_{ctl} = f_{sw} \gg f_0$ by construction. For DDRCC the relative ordering of $f_{ctl}$ and $f_{sw}$ is less clear and depends on topology. The only requirement is that the ripple generated by dithering be sufficiently attenuated at the array terminals to accomplish the goal of increasing effective duty-ratio resolution but not so greatly attenuated that sensing the ripple becomes difficult. For buck MPPTs with conventional filtering, as in [38], the control frequency is electrically limited by the input capacitance and by the rate at which the PWM signal can be changed and is mostly unrelated to the filter characteristics; in that case, $6250 = f_{ctl} \approx f_0$.

By comparison, the moderate-ripple requirement applied to a boost MPPT requires either $f_{ctl} > f_0$ or $f_{ctl} < f_0$. Sampling and PWM limitations imposed by the available microcontroller, an Atmel ATTiny861, yielded the choice of $f_{ctl} = 2 - 5$ Hz. The primary constraint here is ADC noise; significant averaging and consequently significant (order of 100 per point) sampling is necessary for usable results; consequently the microcontroller is sampling for nearly 10% of real time. This dithering frequency is considerably slower than $f_0 = 1$ kHz,[2] so we're not at all effectively increasing the duty-ratio resolution. Applying a ripple waveform to the array to extract power derivatives is certainly still possible at low frequencies, though the algorithm is some-

[1] The MPPT hardware was entirely developed by the author of [37] and [38] Prof. Robert Pilawa when he was a graduate student on MIT's solar car team. He is also the original author of the perturb-and-observe tracking implementation, although others have contributed to different parts of the code base in the $\approx 4$ year history of the MPPT.

[2] Switching frequency $f_{sw}$ for this converter is 31 kHz.

what better described as a hill-climbing algorithm: electrically, the converter is predominantly in steady-state cyclic operation. The 'ripple' imposed on the array in this mode of operation simulates non-steady-state DDRCC or RCC ripple in order to duplicate the control policy.

The purpose of this excursion is not specifically to demonstrate that quasi-DDRCC is the most effective or most efficient controller — as it is almost certainly not — but to demonstrate that the effectiveness of a ripple-sensing control policy can be evaluated independently of the ripple source or timescale.

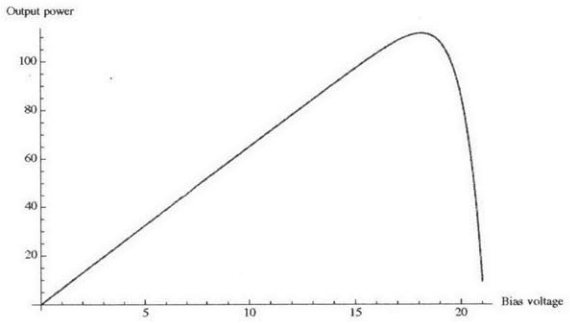


Figure 3-1: Idealized power/bias voltage curve of the PV simulator under test.

### 3.1.2 DDRCC and quasi-DDRCC mode

Unlike perturb-and-observe methods, which switch between 'observe', 'maintain', and occasional 'sweep' states, operation of DDRCC can be iterative and approximately time-invariant. We describe it in pseudocode with Algorithm 1:

**Data**: Desired mean duty cycle, output power, array voltage, current duty cycle
**Result**: Continuous tracking and convergence to a mean duty cycle enforcing the array maximum-power-point
**while** *tracking* **do**
  Dither up and record slope;
  Dither down and record slope;
  Set new desired mean duty cycle;
  Determine dither up and dither down times for next cycle
**end**

**Algorithm 1:** Dithering digital ripple correlation iteration

We make the decision component of this algorithm more explicit in Algorithm 2. In [38] we are given one possible such **ControlPolicy**() for DDRCC. We turn the continuous-time Eqn. 18

**Data**: Desired mean duty cycle, output power, array voltage, current duty cycle
**Result**: Continuous tracking and convergence to a mean duty cycle enforcing the array maximum-power-point
**while** *tracking* **do**
  Dither up and record slope;
  Dither down and record slope;
  New mean duty = **ControlPolicy**(current mean duty, slope measurements);
  Determine dither up and dither down times for next cycle
**end**

**Algorithm 2:** Dithering digital ripple correlation iteration

into discrete-dynamical-system form:

$$D_{t+1} = D_t + k' \operatorname{sgn}(P_{t^+} - P_t) \tag{3.1}$$

with $P_{t^+}$ indicating the power at the midpoint of the dithering cycle. The form of this controller, proportional to a sign rather than to a magnitude, is appropriate in two ways. First, it corresponds to the nature of the measurement as the measurement of a correlation and thus a relative phase: the relative phase between output power and input duty cycle. Second, it provides nondimensionalization of the controller inputs, ensuring that we need not have a power-dependent or unit-of-measurement-dependent gain $k'$, something necessary in perturb-and-observe methods. By making the controller insensitive to slope, we also re-symmetrize the asymmetric 'potential' of the power/bias voltage curve that we are stabilizing, making the same gain appropriate whether we are on the 0 volt or the $V_{oc}$ side of $V_{mpp}$.

We also note that whether the RCC/DDRCC/qDDRCC controller is memoryless is contained in the form of the **ControlPolicy**(). The iterative policy of Equation 3.1 is memoryless, whereas a **ControlPolicy**() containing an independent estimator that refines the best estimate of $(V_{mpp}, I_{mpp})$ and makes an adjustment to the duty cycle based on that would or could contain significant state. Our target operating conditions and time-dependent illumination — dozens or hundreds of slewing femtosatellites in sunlight, eclipse, and penumbra — are poorly characterized. Constellation and satellite attitude control policies are apt to be based on estimates of the current constellation state only, so we enforce this memoryless condition to ensure robustness and convergence are easier to check.

Assuming that a quasi-DDRCC implementation can generate simulated ripple (it can), there is no intrinsic reason why a control policy for RCC or DDRCC should not also work for quasi-DDRCC. Furthermore, Equation 3.1 emphasizes that the heart of DDRCC is a simple discrete-

time proportional controller, with integrated nondimensionalization to boot. Kimball in [39] mentions that "other observer-based solutions that provide signals for the RCC control law are likely to be possible," and that is partly what we explored with quasi-DDRCC.

The quasi-DDRCC algorithm is virtually identical and shares the **ControlPolicy**() function, differing in only the measurement phase, as shown in Algorithm 3.

**Data:** Desired mean duty cycle, output power, array voltage, current duty cycle
**Result:** Continuous tracking and convergence to a mean duty cycle enforcing the array maximum-power-point
Sweep to determine preliminary mean duty ratio;
**while** *tracking* **do**
  **while** *dithering up* **do**
    step through duty ramp;
    record slope
  **end**
  **while** *dithering down* **do**
    step through duty ramp;
    record slope
  **end**
  New mean duty = **ControlPolicy**(current mean duty, slope measurements);
  Determine dither up and dither down times for next cycle
**end**

**Algorithm 3:** Quasi-DDRCC iteration

Because our duty cycle adjustment occurs significantly slower than the input filter corner frequency, two-state duty-cycle dithering does not extract a slope – so we add states, much like the three-way dithering scheme in [37]. In our implementation, we typically stepped through 10 duty cycle steps centered on the desired mean duty cycle, imposing a triangular 'ripple' on the array terminals and measured the difference in output power across each transition of duty cycle. So for each ripple cycle, we collected about 20 measurements of ripple slope and sign.

Multiple measurements necessitate an adjustment to the **ControlPolicy**() of Equation 3.1. The modification is fairly intuitive: we add the signs of the measured slopes over each cycle and apply gain to that:

$$D_{t+1} = D_t + k' \sum_{i}^{N} \mathrm{sgn}(P_{i_{t^+}} - P_{i_t}) \tag{3.2}$$

What's interesting about this is that it seems like a trivial modification: ideally, there's no reason why the signs would differ with $i$. In practice, however, we found our results to be dominated by noise in the measurements, so changes in sign across $i$ were natural. This is actually useful: the addition of noise and therefore the measurement of an *average* sign as the controller input

is an additional dithering that yields useful information. Instead of proceeding at the same rate towards the MPP regardless of distance, the average sign slows the approach as the incremental power increases and therefore average sign approach zero. And because this quantity, too, is dimensionless, the gain can remain constant across different illumination.

So the injection of natural dithering into the estimation portion of the **ControlPolicy**() adds resolution to our location estimate just as deliberate duty-cycle dithering — given appropriate match of filter and ripple design — adds resolution to the array bias.

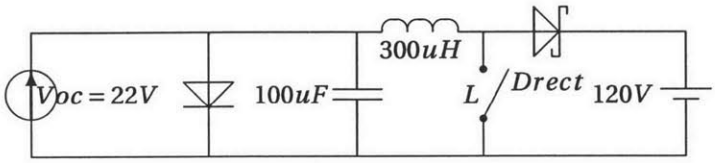


Figure 3-2: Schematic outline of major power components in test apparatus ($V_{oc}$ describes diode array, not current source)

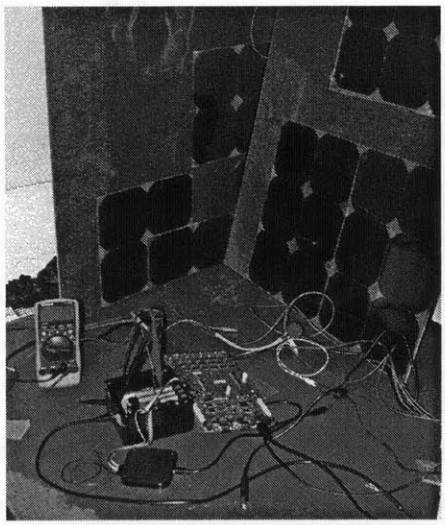

Figure 3-3: Test apparatus. MPPT is the black box in the center.

### 3.1.3 Test setup

A schematic including MPPT components and a picture of the test stand are shown in Figures 3-2 and 3-3. We simulated the photocurrent by forward-biasing an array consisting of 32 SunPower

C50 cells, each with a rated $V_{oc}$ of 0.68 V. The cells were covered to block real photocurrent, so the main time variation remaining is thermal; the cells heat themselves in varying degrees depending on the effectiveness of the power tracking.

The current source was an Agilent CC/CV power supply in constant current mode; in other words, not exceptionally accurate, although we did not encounter any problems attributable to it. We performed testing with simulated array currents between 0.5 and 3.0 A, corresponding to supply current between 1.0 and 6.0 A. This method of testing restricts array current to somewhat less than half of rating in order to not exceed rated diode current or rated MPPT current during array-open or array-short conditions respectively.

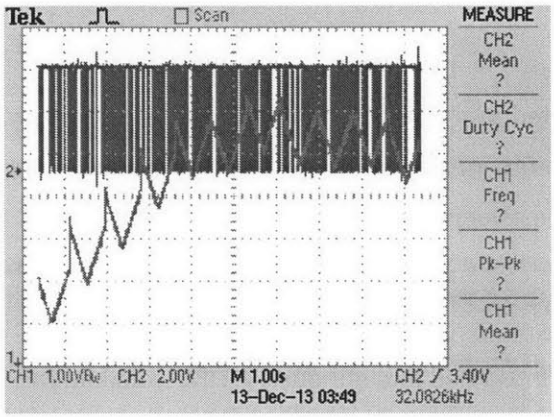


Figure 3-4: Tracking convergence to MPP, demonstrating a cycles-to-convergence consistent with the literature. Array voltage in orange; vastly undersampled PWM signal in turquoise.

The load used for testing was a 5 kWh battery pack consisting of lithium cells in a 31 series configuration. Pack voltage ranged from 117.5 V to 120.2 V during testing. This was used for its low drive impedance, consistency with MPPT design operating conditions,[3] and for its balancing hardware.

Our testing consisted of convergence testing only and refinement of the details and tuned parameters and for lack of time we did not perform any characterization. We did demonstrate that validation of control policies in hardware not purpose-built for DDRCC is a completely viable strategy: the ultimate goal is to assess the practicality of a coordinated dithering strategy, across multiple similarly-illuminated array strings and MPPTs.

Results of the convergence testing were commensurate with that in the literature: conver-

[3] In this case, that we are able to charge it with a total power comparable to the total power output of every femtosatellite in a constellation.

gence within approximately 10 cycles for a constant-voltage-ripple-amplitude method with a 1 V p-p ripple and power feedback by current sensing on the output. This is larger than the ripple magnitudes in [38] by about a factor of 5. The choice of voltage ripple amplitude in dithered ripple correlation methods — in the case of DDRCC by choosing the PWM resolution and the array terminal capacitance, and in the case of q-DDRCC by directly choosing the ripple amplitude — is a topic deserving of further study, since higher ripple would give higher robustness for rapidly-slewing MPP in quickly-varying illumination, and the compromise to power in operating off of MPP decreases as the panel becomes progressively less ideal. Mismatch losses multifurcate the array MPP into several local maxima, flattening the MPP, and resistive losses directly flatten the power/bias curve.

Convergence plots as in Figure 3-4 were virtually identical at mean output power between 10 and 105 watts, as measured with a battery-mounted shunt. This is expected, as the control laws are nondimensional: no first-order variation would be expected, but second-order effects like the greater relative noise power in principle could have affected results.

### 3.1.4 Concessions to non-ideality

The last component we integrated into our quasi-DDRCC method was related to limitations of our testing apparatus: no more than 23 volts of solar cells was available, necessitating MPP operation around 16% duty cycle. We further enforced a restriction that duty cycle could not be less than 10%. This mode of operation was problematic for sweep-based and pure PID tracking, which evaluated the MPP to be at the minimum duty ratio more than half the time at output power of 10 W and about 10% of the time at output power at the maximum 100-110W. Tracking with damping finds the duty ratio limits to be dynamic attractors, since those fixed hard limits minimize the penalty associated with rate of change. To compensate for the closeness of the MPP to the duty ratio limit in dithering mode, we incorporated directional gain control to 'push' the duty ratio away from its travel limits by restricting the cycle-by-cycle slope information collected at apparent[4] duty ratios below minimum. With these conditions, the controller is demonstrably stable with a MPP only 2-3 ripple amplitudes above the lower duty ratio limit, and can escape an initial condition set at the limit, as would happen to the notional satellite when emerging from eclipse.

[4] 'Apparent,' as the duty ratio is hard-limited, but the slope is evaluated between subsequent PWM write commands.

# Chapter 4

# Conclusion

In this report, we have identified the scaling features and characteristics of the existing iEPS voltage conversion stage; in particular, identified necessary changes to the magnetics design and topology for iEPS-type electrospray systems to be implemented on a board-scale femtosat. In the process, we developed a power supply small and simple enough to pose an alternative to large and thermally-unstable high-voltage switches: its total size is less than the high-voltage switch board components on the iEPS PSU. This required us to demonstrate the effectiveness of an unusual autotransformer topology with planar coreless magnetics, at about twice the size necessary for a notional femtosatellite and half the power output required for CubeSat-scale iEPS. In further evidence of the utility of this power supply topology and construction, we showed that femtosatellites incorporating this power supply can maintain near-field communications with no extra hardware, permitting them to do spatial-domain maximum power point tracking.

Satellites at the 'femto-'scale are ready for prime time.

Code for quasi-DDRCC method

```
void DDRCTracking(void){

//      duty_peak = 750;
//      PWMWriteDuty(duty_peak);

        /*We start here with and at the sweep max power point, duty_peak,
             a */
        uint16_t duty_center = duty_peak;
        uint16_t old_duty_center = duty_center;
//      duty_center = 512;
//      PWMWriteDuty(duty_center);

        //DITHERING PROPERTIES (secular)
        uint16_t dither_amplitude = 100;
        uint16_t dither_sample_amplitude = 1;
        uint8_t dither_sample_count_orig = 10;
        uint8_t dither_sample_count = dither_sample_count_orig;
        uint8_t dither_sample_interval = 10; //milliseconds
        uint16_t orig_gain = 1;
        uint16_t up_slope_gain = orig_gain;
        uint16_t down_slope_gain = orig_gain;
        uint16_t duty_center_diff = 0;
        uint8_t center_diff_zeroes = 0;

        vin=ADCReadValue(VIN_MUX,VIN_READINGS);
        vout=ADCReadValue(VOUT_MUX,VOUT_FAST_READINGS);
        vin_adjusted=vin*VREF/ADC_MAX*VIN_DIVIDER/VIN_READINGS;
        vout_adjusted=vout*VREF/ADC_MAX*VOUT_DIVIDER/VOUT_FAST_READINGS;

        while(vin_adjusted > VIN_MIN && vout_adjusted < VOUT_MAX &&
            vout_adjusted > VOUT_MIN){
                /*clear the non-secular parts of our state*/
                uint8_t dither_up_positive = 0;
                uint8_t dither_down_positive = 0;
                int16_t dither_up_islope = 0;
                int16_t dither_down_islope = 0;
```

```
        /*Check that secular parameters are in range*/
        if(duty_center + up_slope_gain*dither_sample_count >
            DUTY_MAX){
                up_slope_gain = 1;
                down_slope_gain = 1;
                dither_sample_count = dither_sample_count_orig
                    >>2;
        }
        else {
                up_slope_gain = orig_gain;
                down_slope_gain = orig_gain;
                dither_sample_count = dither_sample_count_orig;
        }

        if(duty_center - down_slope_gain*dither_sample_count <
            DUTY_MIN){
                down_slope_gain = 1;
                up_slope_gain = 1;
                dither_sample_count = dither_sample_count_orig
                    >>1;
        }
        else {
                down_slope_gain = orig_gain;
                up_slope_gain = orig_gain;
                dither_sample_count = dither_sample_count_orig;
        }
        /*First, we dither up:*/
//      iout = ADCReadValue(IOUT_MUX,IOUT_READINGS);
//      PWMWriteDuty(dither_amplitude + duty_center);

        /*Now sample for the slope of the output ripple*/
        uint8_t i = 0;
        for( i = 0; i <= dither_sample_count; i++){
                //current ripple
                iout = ADCReadValue(IOUT_MUX,IOUT_FAST_READINGS);

                if(duty_center == DUTY_MIN){
                        PWMWriteDuty(i*dither_sample_amplitude +
                            duty_center);
```

```
                }
                else if(duty_center == DUTY_MAX){
                        PWMWriteDuty(i*dither_sample_amplitude +
                            duty_center - dither_sample_count*
                            dither_sample_amplitude);
                }
                else{
                        PWMWriteDuty(i*dither_sample_amplitude +
                            duty_center - dither_sample_count*
                            dither_sample_amplitude/2);
                }
                delayms(dither_sample_interval);
                int16_t interval_islope = (int16_t)((ADCReadValue
                    (IOUT_MUX,IOUT_FAST_READINGS) - iout)>>
                    ISLOPE_SHIFT);
                if(interval_islope > 0){
                        dither_up_positive++;
                }
                dither_up_islope = dither_up_islope +
                    interval_islope;
        }

        /*now dither down:*/
//      iout = ADCReadValue(IOUT_MUX,IOUT_READINGS);
//      PWMWriteDuty(duty_center - dither_amplitude);
        /*Now sample for the slope of the output ripple*/
        i = 0;
        for( i = 0; i <= dither_sample_count; i++){
                //current ripple
                iout = ADCReadValue(IOUT_MUX,IOUT_FAST_READINGS);
                if(duty_center == DUTY_MIN){
                        PWMWriteDuty( duty_center - i*
                            dither_sample_amplitude +
                            dither_sample_count*
                            dither_sample_amplitude);
                }
                else if(duty_center == DUTY_MAX){
                        PWMWriteDuty( duty_center - i*
                            dither_sample_amplitude -
```

```
                        dither_sample_count*
                        dither_sample_amplitude);
                }
                else{
                        PWMWriteDuty( duty_center - i*
                        dither_sample_amplitude +
                        dither_sample_count*
                        dither_sample_amplitude/2 );
                }

                delayms(dither_sample_interval);
                int16_t interval_islope = (int16_t)((ADCReadValue
                    (IOUT_MUX,IOUT_FAST_READINGS) - iout)>>
                    ISLOPE_SHIFT);
                if(interval_islope > 0){
                        dither_down_positive++;
                }
                dither_down_islope = dither_down_islope +
                    interval_islope;
        }


        /*calculate ripple amplitude and phase and set new center
            */
        if(dither_up_islope > dither_down_islope){
//              duty_center = duty_center + up_slope_gain       *
      dither_up_islope;
                duty_center = duty_center + up_slope_gain       *
                      (uint16_t) (dither_up_positive -
                    dither_down_positive);
                if(duty_center > DUTY_MAX){
                        duty_center = DUTY_MAX;
                }
                else if(duty_center < DUTY_MIN){
                        duty_center = DUTY_MIN;
                }

                duty_center_diff =  duty_center - old_duty_center
                    ;
```

```
        }
        else if(dither_up_islope < dither_down_islope){
//              duty_center = duty_center - down_slope_gain *
    dither_down_islope;
                duty_center = duty_center - down_slope_gain * (
                    uint16_t) (dither_down_positive -
                    dither_up_positive);

                if(duty_center > DUTY_MAX){
                        duty_center = DUTY_MAX;
                }
                else if(duty_center < DUTY_MIN){
                        duty_center = DUTY_MIN;
                }
                duty_center_diff = old_duty_center - duty_center;
        }
        else if(dither_up_islope == dither_down_islope){
                duty_center_diff = 0;
        }

        old_duty_center = duty_center;


        /*tweak secular parameters to aid convergence - the
            derivative part of the controller*/
        if(duty_center_diff <= CENTER_DIFF_LOWER_THRESHOLD){
                if(center_diff_zeroes <= CENTER_DIFF_STACKLENGTH)
                    {
                        center_diff_zeroes++;
                }
        }
        else if(duty_center_diff > CENTER_DIFF_UPPER_THRESHOLD){
                if(center_diff_zeroes > 0){
                        center_diff_zeroes = 0;
                }
        }
        if(duty_center == DUTY_MAX || duty_center == DUTY_MIN){
                center_diff_zeroes = 0;
        }
```

```
                switch(center_diff_zeroes){
                                //this component is occasionally
                    problematic
                            case 40:
                            dither_sample_count = MIN_SAMPLE_COUNT;
                            dither_sample_interval = 1;
                            break;
                        case 10:
                            dither_sample_count = MIN_SAMPLE_COUNT*3;
                            dither_sample_interval = 1;
                            break;
                        case 0:
                            dither_sample_count =
                                dither_sample_count_orig;
                            dither_sample_interval = 1;
                            break;
                }



                /*idle if off*/
                vin=ADCReadValue(VIN_MUX,VIN_READINGS);
                vout=ADCReadValue(VOUT_MUX,VOUT_FAST_READINGS);
                vin_adjusted=vin*VREF/ADC_MAX*VIN_DIVIDER/VIN_READINGS;
                vout_adjusted=vout*VREF/ADC_MAX*VOUT_DIVIDER/
                    VOUT_FAST_READINGS;
                if (!(vin_adjusted > VIN_MIN && vout_adjusted < VOUT_MAX
                    && vout_adjusted > VOUT_MIN))
                {
                        PWMDisable();
                        break;
                }

        }
        PWMDisable();
}
```

# Bibliography


[1] Lozano, P. and Courtney, D., "On the development of high specific impulse electric propulsion thrusters for small satellites," *Small Satellites and Services 2010 "The 4S Symposium"*, 2010.

[2] F Martel, L Perna, P. L., "Minature ion electrospray thrusters and performance tests on CubeSats," *26th Annual AIAA/USU Conference on Small Satellites*, 2012.

[3] IXYS Corporation, *IXTH03N400 High Voltage Power MOSFETS: IXTV03N400S preliminary technical information.*

[4] *IPC-2221 Generic Standard on Printed Board Design*, IPC Association, November 2012.

[5] Electronics, P., January 2014.

[6] "Flyback converter, Wikipedia," .

[7] Manchester, Z., "KickSat – Your personal spacecraft in space!" Kickstarter.com.

[8] Personal conversation with Paulo Lozano, June 2013.

[9] "CubeSat Design Specification," Tech. rep., California Polytechnic State University, February 2014.

[10] "Program Level Poly-Picosatellite Orbital Deployer (PPOD) and CubeSat Requirements Document," Tech. Rep. LSP-REQ-317.01, National Aeronautics and Space Administration, October 2011.

[11] Williams, W. D., "Unusual Small Satellite Applications," *International Communications Satellite Systems Conference*, No. 31, AIAA, 2013.

[12] "CubeSat.Org: Falcon 9 CRS-3 Launch 2014," .

[13] Tristancho, J., *Implementation of a femto-satellite and a mini-launcher*, Master's thesis, Universitat Politecnica de Catalunya, May 2010.

[14] D Barnhart, T Vladimirova, A. B., "Very-small-satellite design for distributed space missions," *Journal of Spacecraft and Rockets*, Vol. 44, No. 6, 2007, pp. 1294–1306.

[15] Tristancho, J. and Gutierrez-Cabello, J., "A probe of concept for femto-satellites based on commercial-of-the-shelf," *IEEE/AIAA 30th Digital Avionics Systems Conference (DASC)*, 2011, pp. 8A2–1–8A2–9.

[16] D Barnhart, T Vladimirova, A. B., "A low-cost femtosatellite to enable distributed space missions," Tech. rep., The Department of the Air Force, 2006.

[17] Weis, L. and Peck, M., *Attitude Control for Chip Satellites using Multiple Electrodynamic Tethers*, American Institute of Aeronautics and Astronautics, 2014/05/17 2012.

[18] Manchester, Z. and Peck, M., *Stochastic Space Exploration with Microscale Spacecraft*, American Institute of Aeronautics and Astronautics, 2014/05/17 2011.

[19] Reichbach, J., *Micropropulsion System Selection for Precision Formation Flying Satellites*, Master's thesis, Massachusetts Institute of Technology, January 2001.

[20] Atchison, J. A. and Peck, M. A., "A passive, sun-pointing, millimeter-scale solar sail," *Acta Astronautica*, Vol. 67, No. 1–2, 2010/8// 2010, pp. 108–121.

[21] Atchison, J. and Peck, M., "A Millimeter-Scale Lorentz-Propelled Spacecraft," *Guidance, Navigation and Control Conference and Exhibit*, No. 6847, AIAA, August 2007.

[22] Atchison, J. and Peck, M., "Length Scaling in Spacecraft Dynamics," *Journal of Guidance, Control, and Dynamics*, Vol. 34, No. 1, January-February 2011, pp. 231–246.

[23] Wertz, J. R. and Larson, W. J., editors, *Space Mission Analysis and Design*, Space Technology Series, Microcosm Press, 3rd ed., 1999.

[24] Taylor, G., "Disintegration of water drops in an electric field," *Proceedings of the Royal Society of London. Series A, Mathematical and Physical Sciences*, Vol. 280, No. 1382, July 1964, pp. 383–397.

[25] T Roy, V Hruby, N. R., "CubeSat propulsion using electrospray thrusters," *23rd Annual AIAA/USU Conference on Small Satellites*, Busek Co. Inc., 2009.

[26] Phinney, J. W., *Multi-resonant passive components for power conversion*, Ph.D. thesis, Massachusetts Institute of Technology, Department of Electrical Engineering and Computer Science, http://hdl.handle.net/1721.1/33859, 2005.

[27] Cockcroft, J. D. and Walton, E. T. S., "Experiments with High Velocity Positive Ions. (I) Further Developments in the Method of Obtaining High Velocity Positive Ions," *Proceedings of the Royal Society of London. Series A*, Vol. 136, No. 830, 1932, pp. 619–630.

[28] Makowski, M. and Maksimovic, D., "Performance limits of switched-capacitor DC-DC converters," *PESC '95 Record., 26th Annual IEEE Power Electronics Specialists Conference*, Vol. 2, 1995, pp. 1215–1221.

[29] Venkatachalam, K., Sullivan, C., Abdallah, T., and Tacca, H., "Accurate prediction of ferrite core loss with nonsinusoidal waveforms using only Steinmetz parameters," *Computers in Power Electronics, 2002. Proceedings. 2002 IEEE Workshop on*, 2002, pp. 36–41.

[30] Li, Q., Lim, M., Sun, J., Ball, A., Ying, Y., Lee, F., and Ngo, K. D. T., "Technology road map for high frequency integrated DC-DC converter," *Applied Power Electronics Conference and Exposition (APEC), 2010 Twenty-Fifth Annual IEEE*, 2010, pp. 533–539.

[31] Kelly, S., Collins, C., Duffy, M., Rhen, F. M. F., and Roy, S., "Core Materials for High Frequency VRM Inductors," *Power Electronics Specialists Conference, 2007. PESC 2007. IEEE*, 2007, pp. 1767–1772.

[32] Cuk, S.; Middlebrook, R. D., "A general unified approach to modelling switching dc-to-dc converters in discontinuous conduction mode," *Power Electronics Specialists Conference*, June 1977, pp. 36–57.

[33] "EPC2012 Datasheet," data sheet, Efficient Power Conversion, 2012.

[34] Kotte, H., Ambatipudi, R., and Bertilsson, K., "High speed cascode flyback converter using multilayered coreless printed circuit board (PCB) step-down power transformer," *IEEE 8th International Conference on Power Electronics and ECCE Asia (ICPE ECCE)*, 2011, pp. 1856–1862.

[35] "Antennas for RFIC Transmitters and Receivers," Tech. rep., RFM/Murata, 2007.

[36] Esram, T. and Chapman, P., "Comparison of Photovoltaic Array Maximum Power Point Tracking Techniques," *Energy Conversion, IEEE Transactions on*, Vol. 22, No. 2, 2007, pp. 439–449.

[37] Barth, C. and Pilawa-Podgurski, R., "Dithering digital ripple correlation control for photovoltaic maximum power point tracking," *Power and Energy Conference at Illinois (PECI), 2013 IEEE*, 2013, pp. 36–41.

[38] Barth, C. and Pilawa-Podgurski, R., "Implementation of dithering digital ripple correlation control for PV maximum power point tracking," *Control and Modeling for Power Electronics (COMPEL), 2013 IEEE 14th Workshop on*, 2013, pp. 1–7.

[39] Kimball, J. and Krein, P., "Discrete-Time Ripple Correlation Control for Maximum Power Point Tracking," *Power Electronics, IEEE Transactions on*, Vol. 23, No. 5, 2008, pp. 2353–2362.

[40] Pilawa-Podgurski, R., Sagneri, A., Rivas, J., Anderson, D., and Perreault, D., "Very High Frequency Resonant Boost Converters," *Power Electronics Specialists Conference, 2007. PESC 2007. IEEE*, 2007.

[41] Neugebauer, T. and Perreault, D., "Filters with inductance cancellation using printed circuit board transformers," *Power Electronics Specialist Conference, 2003. PESC '03. 2003 IEEE 34th Annual*, 2003.

[42] Mino, M., Yachi, T., Tago, A., Yanagisawa, K., and Sakakibara, K., "A new planar microtransformer for use in micro-switching converters," *IEEE Transactions on Magnetics*, 1992.

[43] Ouyang, Z. and Andersen, M., "Overview of Planar Magnetic Technology — Fundamental Properties," *IEEE Transactions on Power Electronics*, 2013.

[44] Mohan, S., "Simple Accurate Expressions for Planar Spiral Inductances," *IEEE Journal of Solid-State Circuits*, Vol. 34, No. 10, October 1999.